Lithium trapping as a degradation mechanism of the electrochromic properties of all-solid-state WO_3//NiO devices†

Dongmei Dong,[a] Wenwen Wang,[a] Aline Rougier,[b] Antoine Barnabé,[c] Guobo Dong,[a] Fan Zhang[a] and Xungang Diao *[a]

There has been keen interest for years in the research of all-solid-state transmittance-type electrochromic (EC) devices due to their various applications especially in "smart windows". A step forward has been taken in the successful preparation of full multilayered devices with enlarged optical contrast and fast switching response. However, limited durability remains a severe issue. Upon cycling, EC devices suffer from decline of charge capacity as well as optical modulation while the detailed degradation mechanisms remain poorly understood. Here, we demonstrate unambiguous ion-trapping evidence to interpret the charge density decay of the EC device induced using various voltammetric cycling protocols, namely long-term cycling and accelerated cycling. Pronounced comparable ion trapping occurs in cathodically colored WO_3 films whatever the cycling procedure is, suggesting the existence of the trapping "saturation" phenomenon. From second-ion-mass-spectroscopy analysis, the $^{7}Li^{+}/^{184}W^{+}$ ratio in the degraded WO_3 films is more than 100 while it is almost zero in the as-prepared films. In contrast, for anodically colored NiO, a larger number of trapped cations is determined in the long-term cycled films than in the accelerated ones. In combination with X-ray-photoelectron-spectroscopy, variable bonding energies indicate that the ions are trapped at different types of sites, depending on the cycling procedure, and they can reside in the structural channels or break the network chains to form new chemical bondings, thus resulting in a significant color difference. In addition, a clear upward trend in the trapped Li concentration along with depth is observed. All our findings provide a deep insight into the degradation phenomenon taking place in electrochromic films as well as in full devices and offer valuable information for the understanding of micro mechanisms.

DOI: 10.1039/c8tc01372a

1. Introduction

Electrochromism is defined as a phenomenon in which a change in color takes place in the presence of an applied voltage and which involves the reversible insertion/de-insertion of ions within the film structure under electric potential.[1–3] Most electrochromic devices (ECDs) for practical applications use a cathodically coloring tungsten oxide (WO_3) thin film separated from an anodically coloring nickel oxide (NiO) thin film by an electrolyte in a thin-film-form or as a polymer layer, and this sandwich-like configuration is embedded between transparent conductive films functioning as electrodes.[4–6] WO_3, presenting lattice channels, consists of clusters with corner-sharing WO_6 octahedra, linked together by W–O–W bonds[7] while W═O bonds involving terminal oxygen at the surface of the clusters are often characteristic of the disordered phase. Depending on the tilting angles of WO_6, the oxide can adopt monoclinic, triclinic, orthorhombic, tetragonal and cubic crystalline structures[8] or it can be amorphous with the same but randomly oriented building units (WO_6, WO_5, WO_4, *etc.*).[9] The coloration of WO_3 films takes place by charge transfer between W^{6+} and W^{5+} sites. Crystalline NiO has a rock salt structure with one Ni atom and one O atom in a cubic unit cell and it is a p-type semiconductor with cationic vacancies linked with the formation of Ni^{3+}.[4] Electrochromic (EC) coloration and bleaching in NiO films occur by extraction and insertion of 3d electrons in the valence band without affecting the metal–oxygen bond,[10] and the optical absorbance in the colored state results from the charge transfer from Ni^{2+} to Ni^{3+} sites. Even in the full ECD, optical modulation occurs when ions typically Li^{+} are shuttled between WO_3 and NiO films accompanied by charge-balancing

[a] *Electrochromic Center, School of Physics and Nuclear Energy Engineering, Beihang University, Beijing 100191, P. R. China. E-mail: diaoxg@buaa.edu.cn*

[b] *CNRS, Univ. Bordeaux, ICMCB, UMR 5026, F-33600 Pessac, France*

[c] *CIRIMAT, Université de Toulouse, CNRS, Université Toulouse 3 Paul Sabatier, 118 route de Narbonne 31062, Toulouse Cedex 9, France*

† Electronic supplementary information (ESI) available. See DOI: 10.1039/c8tc01372a

insertion/extraction of electrons under a potential applied to the electrodes.[11]

The optical transmittance of the ECD can be reversely changed by repeated charge and electron exchange and the EC properties can remain constant without any negative changes emerging within the device. The insertion and extraction of Li cations in WO_3 and NiO thin films are significantly influenced by many factors including their structure, surface, composition characteristics and so on.[12,13] Upon cycling, these characteristics cannot be precisely kept the same. As a result, it is believed that not all the injected cations can reversibly successfully ''escape'' from the EC films upon extended electrochemical cycling, thus causing a related ion trapping problem[14] and impairing the charge capacity as well as the optical modulation range. If shrinkage of the ECD optical modulation is due to an increase in the transmittance in the colored state, it corresponds to a critical decrease of the amount of Ni^{3+} (brownish) or W^{5+} (blue) or both. Reversely, if the device suffers from the decrease in transmittance in the bleached state, then it indicates a decrease of the amount of Ni^{2+} (transparent) or W^{6+} (transparent). There are already several studies on long-term durability problems in a single EC film, mostly, WO_3,[15] but the decay of charge density and optical modulation for the full ECD nevertheless remains poorly understood. Thus the interpretation of the mechanism guiding the declining process is challenging from both theoretical and experimental perspectives.

In this study, we present results from a comprehensive investigation on the role of cathodic WO_3 and anodic NiO films' structure, composition and surface chemistry played in the full device's degradation mechanism upon electrochemical cycling. For this purpose, we realize the ECD degradation using two protocols of voltammetric cycling: (i) conventional life-time extensive measurements at a high scan rate of 100 mV s^{-1} and (ii) accelerated short-term harsh measurements at relatively low scan rates decreasing from 50 to 1 mV s^{-1}. Wen *et al.*[14] have recently reported that the ion trapping accounts for the EC performance decay. Here, time-of-flight secondary ion mass spectrometry (ToF-SIMS) is used to provide unambiguous evidence for the Li cation trapping in films. Indeed, we show a comparable Li trapping level in degraded WO_3 films whatever the voltammetric cycling protocol is, indicative of the basic trap saturation in films independent of degradation modes. For WO_3 films subjected to different degradation processes, such a saturation phenomenon will lead to comparability in the amounts of trapped Li^+ ions, but the nature of cations' trapping sites is not of the same type, supported by the chemical bonding's binding energy shift. Interestingly, for the Li trapping level, a different behavior is observed in anodic NiO. A larger quantity of trapping cations is determined in the first type of cycling (*i.e.* conventional life time extensive measurements). Furthermore, a depth-dependent distribution is found in Li concentration. The present work on degradation mechanism in a full device is a continuation of earlier studies of ours[16–19] showing enhanced EC performance such as enlarged optical contrast, fast switching response and improved durability, and it goes far beyond the previous discussion of degradation dynamics in single layers.[20]

2. Experimental

2.1 Fabrication of ECDs and electro-optical measurements

Single layers of WO_3 and NiO were prepared prior to their integration in full ECDs. Both of the two films were deposited by reactive direct current magnetron sputtering from W and Ni targets (60 mm in diameter and 3 mm in thickness), respectively, in a mixture of oxygen and argon at room temperature. Thin films were deposited onto commercial Indium Tin Oxide (ITO) glass substrates, using a target-to-substrate separation distance of 17 cm, and the holder rotating on its symmetrical axis at a constant speed to ensure the uniformity of the films in the sputtering process. More details on optimized EC film deposition parameters are provided in Table 1. Additionally, for the electrolyte, a mixture of polyurethane acrylate (PUA)-based UV curing adhesive and 1 M $LiClO_4$ propylene carbonate (PC) ionic liquid with a specific ratio of 2 : 1 was prepared in advance.

The ECD was composed of WO_3 as a cathodic electrode, a $LiClO_4$–PC gel polymer as an electrolyte, and NiO as an anodic electrode. A hollow frame of two electrochromic single layers on glass was prepared for the perfusion of the electrolyte mixture. Epoxy adhesive was used as a sealer to avoid liquid leakage. After the perfusion, the frame full of the electrolyte mixture was exposed to two parallel UV light sources (Philips, 8 W) for 20 minutes to ensure complete curing. The device fabrication conditions are summarized in Table 2. A series of three devices were prepared with exactly the same parameters and at the same time. ECDs were labelled ECD1, ECD2 and ECD3. Cyclic voltammetry (CV) measurements were conducted with different scan rates. In order to obtain a fully complete cycle, the voltammetric cycling started from the initial potential of 0 V and ended at the final potential of 0 V. For ECD 2 and 3, at a potential of 0 V, the coloring procedure is nearly finished and the bleaching step is ready to begin next. For reference purposes, ECD1 was as prepared without applying any electrochemical cycling. Long-term cycling was carried out on ECD2 in the potential range of $\pm$1.8 V with a fast scan rate of 100 mV s^{-1} for over 21 316 cycles. In contrast, a continuously decreasing scan rate from 50 to 1 mV s^{-1} with the same potential range was applied on ECD3 in order to accelerate the degradation process. To allow comparison, the initial and end voltages applied to ECD 2 and 3 were controlled absolutely identical. Following the cycling step, the 3 ECDs were opened and 6 samples were released for the convenience of further study. They were named

Table 1 Detailed deposition parameters of the single layers WO_3 and NiO

Target	Power source	Pressure (Pa)	$Ar : O_2$	Power (W)	Time (min)	Thickness (nm)
W	DC	1.7	200 : 80	480	50	600
Ni	DC	2.4	200 : 3	320	50	500

Table 2 Fabrication conditions of ECDs and their corresponding EC layers after degradation

Cathodic electrode	Electrolyte	Anodic electrode	ECD	CV parameter for ECD			Sample
				E/V	Scan rate/mV s^{-1}	Cycle	
WO_3	$LiClO_4$(PC) UV-curing adhesive	NiO	ECD1	0	0	0	WO_3-1 NiO-1
			ECD2	1.8	100	21 316	WO_3-2 NiO-2
			ECD3	1.8	50 to 1	160	WO_3-3 NiO-3

WO_3-1 and NiO-1 (from ECD1); WO_3-2 and NiO-2 (from ECD2); and WO_3-3 and NiO-3 (from ECD3), respectively.

2.2 Characterization of device degradation

Measurements on the ECDs by cyclic voltammetry (CV) were carried out by using a conventional two-electrode configuration in a CHI 660E electrochemical workstation (Chen Hua Instruments, made in Shanghai, China) in normal ambient air. *In situ* and *ex situ* optical transmittance of the films was recorded on a Jasco V-570 spectrophotometer. The underlying causes of the charge density and optical property degradations were explored by Grazing Incidence X-Ray Diffraction (GIXRD), Raman Spectroscopy (RS), Atomic Force Microscopy (AFM), Scanning Electron Microscopy (SEM), Focused Ion Beam (FIB) and Second Ion Mass Spectroscopy (SIMS) in combination with X-ray Photoelectron Spectroscopy (XPS) which allowed us to get near to microscopic mechanisms for the charge density decay. GIXRD and RS were used for the structural characterizations. GIXRD patterns were recorded on a Rigaku D/Max 2200 diffractometer using a Cu K_α source ($\lambda_{Cu\text{-}K\alpha1}$ = 1.5418 Å) with a small incident grazing angle α of 0.3 degree. RS signals were collected under ambient conditions using a Horiba Jobin Yvon LabRAM spectrometer equipped with a fiber coupled 532 nm laser. The surface topography and roughness (R) of the films were observed using an instrument Nanosurf Easyscan AFM from Bruker, operating with NanoScope Analysis software. Meanwhile, the surface morphologies and microstructures of WO_3 and NiO films were also characterized using a Field Emission Gun (FEG)-SEM (JEOL JSM 7800F Prime) and an FEG-SEM/FIB apparatus (FEI Helios Nanolab600i dual beam) operating at 30 kV. In order to get an insight into the microstructure situation beneath the surface, Focused Ion Beam (FIB) was used for observing the cross cut section of the multilayered device. A 1.2 μm layer of Pt was coated on the top to prevent damage from FIB milling and a lamella is produced. Elemental compositions and valence states were determined by SIMS and XPS using an ION-TOF GmbH TOF.SIMS 5–100 and a Thermofisher ESCALAB 250Xi apparatus, respectively. Carbon was used as the calibration source in the XPS measurement and the binding energies of all samples were set by fixing the C 1s peak at 284.8 eV for comparison. SIMS analysis was performed using Bi^+ primary ions at an energy of 30 keV, with the scanning area and the incidence angle being 100 μm × 100 μm and 45 degree, respectively. The second ions were positive with mass ranging from 0 to 1000 amu. Depth profiles of positive ions were obtained in the interlaced mode using O_2^+ ions at 2 keV.

3. Results and discussion

3.1 Effects of electrochemical cycling on the full device

The ECD consists of a cathodic EC layer WO_3 on the transparent electrode ITO, an anodic EC layer NiO on ITO, and between them a gel polymer electrolyte containing Li cations and anions (Fig. S1, ESI†). It is widely accepted that the EC effect involves the simultaneous insertion/extraction of electrons provided by an external potential and Li cations from the electrolyte and the subsequent formation of coloring centers W^{5+} and Ni^{3+} or bleaching W^{6+} and Ni^{2+}.[21] The cathodic tungsten oxide film with high transparency in the oxidized state W^{6+} shows a blue color when it is reduced, or *vice versa*, and the anodic nickel oxide film show opposite electrochromism to the former, and it turns brownish due to Ni^{3+} states accompanying the extraction of electrons and Li^+.

The first step in our work consisted of the degradation of the devices ECD2 and ECD3 using two voltammetric cycling modes as explained in the Introduction section. The first type is conventional long-term life-time extensive cycling applied on ECD2 while for comparison the second is accelerated harsh voltammetric cycling applied on ECD3, and at the same time, ECD1 just prepared as a blank sample without cycling. The difference in the cycling mode lies in the scan rate which determines the time for bleaching/coloring. The fast scan rate applied in ECD2 corresponds to a short time for bleaching/coloring, while the slow scan rates in ECD3 correspond to a longer time for bleaching/coloring. Fig. 1a shows typical *CV* curves for ECD2 with a constant scan rate of 100 mV s^{-1}. One cycle lasts 72 s : 36 s for bleaching and another 36 s for coloring. The CV curves show a steady change upon cycling. The area of the *CV* curve decreases with an increase in the number of cycles. Considering that the scan rate is kept constant, the shrinkage trend in the *CV* characteristics indicates that less charges are capable of moving within the device structure, indicative of the device degradation. As shown in Fig. 1b and c, upon cycling, the reduction/oxidation peaks shift towards a higher potential direction (marked with ''star'' and ''arrow'') and become less pronounced, characteristics of voltammetric cycling declination. The reduction/oxidation activities are depressed and there is shrinkage in the charge capacity. On the one hand, the redox peaks show decreasing values of current density,

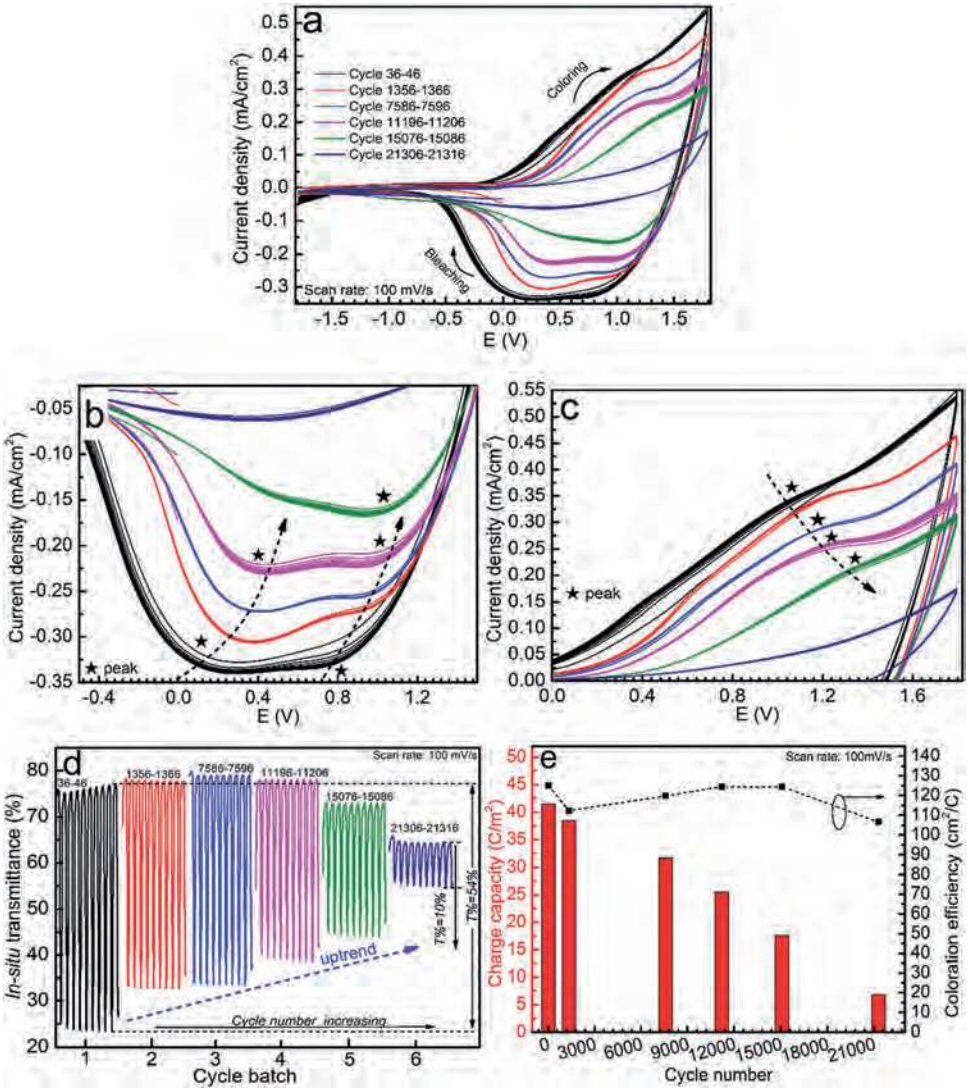

Fig. 1 (a) CV data of ECD2 for the chosen cycles at a constant scan rate of 100 mV s^{-1} recorded in the potential window of ±1.8 V; a magnified view of the (b) cathodic and (c) anodic peak evolution in CVs; (d) *in situ* optical transmittance of ECD2 at 550 nm; (e) charge capacity and coloration efficiency variations with regard to the cycle number for ECD2.

which demonstrates a slowing diffusion kinetics of Li^+ ions in the electrochromic films for the bleaching and coloring.[22] On the other hand, a higher potential is required to provide more energy to overcome the energy barrier to maintain the electrochemical reaction. The relationship between the potential shift and the polarization of electrochromic layers was already reported by various authors.[23–25] In combination with *in situ* transmittance evolution of some chosen cycles presented in Fig. 1d, gradual degradation does occur with transmittance modulation decreasing from 54% to 10%. In general, the basic degradation of devices results from a decreased transmittance in bleached states, an increased transmittance in colored states or a combination of both. Here, the increased transmittance in colored states is the main reason for ECD2 decay. This degradation behavior can be defined as ''uptrend degradation''. This degradation form refers to the transmittance curve of EC films and devices as a whole appearance upward trend upon cycling. Charge density exchange directly affects the optical modulation of NiO and WO_3 films since it represents the amount of charge-compensating electrons that are inserted or extracted in one CV cycle and alter the position of the Fermi level in the valence band.[4] In our work, in ECD2, we found that the experimental decay of charge density leads to a higher transparency overall for both bleached and colored states, which is described as ''upwards degradation trend''. Hence, the charge decay must be associated with a decrease of the number of Ni^{3+} (and/or W^{5+}) and an increase of the Ni^{2+} (and/or W^{6+}). It can be reckoned that compounds formed after long-term multiple electrochromic reactions must be divalent with respect to Ni (and/or W^{6+}). Furthermore, more Li^+ ions are evidenced to be trapped in the NiO layer (see discussions below), which will cause the reduction of Ni^{3+} (brown) and the formation of Ni^{2+} (transparent), thus leading to a transmittance increase overall.

It is very interesting to note that after ~11 000 cycles not only the colored but also the bleached state is now degrading,

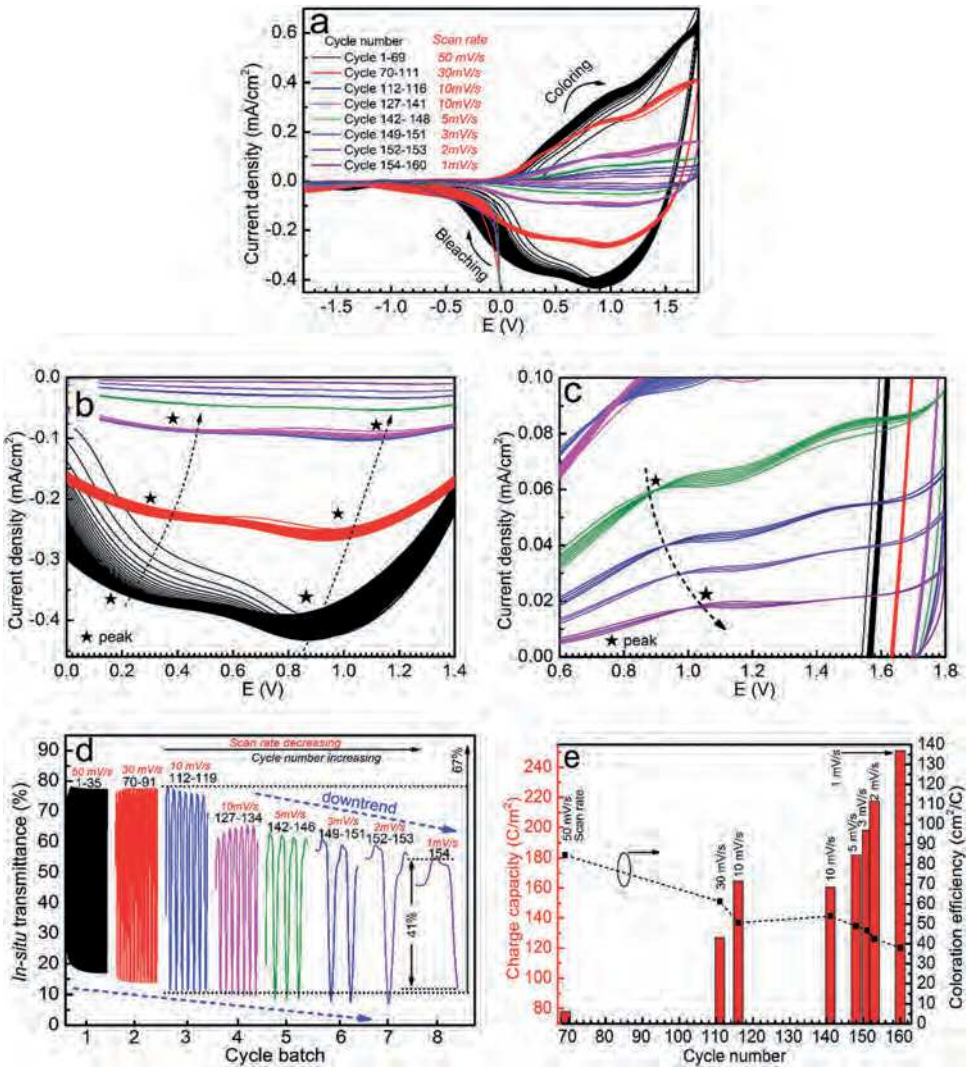

Fig. 2 (a) CV data of ECD3 for the chosen cycles at variable scan rates decreasing from 50 to 1 mV s^{-1} recorded in the potential window of ±1.8 V; a magnified view of the (b) cathodic and (c) anodic peak evolution in CVs; (d) *in situ* optical transmittance of ECD3 at 550 nm; (e) charge capacity and coloration efficiency variation with regard to the cycle number as well as the scan rate for ECD3.

which differs from the above observations. Evidently, for the conventional long-term degradation protocol with a fast scan rate, more time is required to affect the bleached state than the colored one. It has been pointed out[26] that the behavior of ''deep'' traps could be responsible for degrading the bleached state. And, in Fig. 2a, after ~100 cycles, the bleached state starts to suffer from the harsh cycling, indicative of the similarity between the degradations in the two protocols.

To further investigate the ''uptrend degradation'' evolution, the charge capacity (Q) referred to the ability of holding guest charges and coloration efficiency (CE) representing the optical change induced by per unit charge are also calculated as shown in Fig. 1e.

$$Q = \int (j\mathrm{d}V)/s; \quad \mathrm{CE} = \log(T_b/T_c)/Q$$

where j is the current density (mA cm^{-2}), V is the potential (V), s is the scan rate (mV s^{-1}), and T_b/T_c is the ratio of bleached/colored transmittances.[27] Q decreases from 42 C m^{-2} for the 46th cycle to 7 C m^{-2} after the last cycle 21 316th at a constant scan rate of 100 mV s^{-1}. That is, ECD2 has been cycling for 426.32 h continuously with 83.3% capacity decay. As expected, this is a typical degradation performance of conventional long-term voltammetric cycling. Surprisingly, the CE values are relatively stable at 117 ± 9 cm^2 C^{-1} during such long-time cycling, suggesting that the ability of per unit active charge to realize optical modulation remains unchanged. So the ECD2 degradation is attributed to the significant decrease in the amount of moving charges upon cycling, and it would well fit with decohesion of the film to be discussed in FIB analysis.

To further understand the electrochromic device degradation behavior, a comparison method is used. ECD3 is subjected to harsh CV cycles to purposely degrade it. ECD2 and 3 are compared when considering at the same potential and at the same state they are stopped upon cycling. The same potential range of ±1.8 V but with a scan rate changed every 10 000 s

from 50 mV s^{-1} to 1 mV s^{-1} is applied on ECD3 (Fig. 2a). The bleaching/coloring time increases from 72 to 3600 s in this measurement. The disappearance of anodic/cathodic peaks as shown in the enlarged images in Fig. 2b and c is an illustration of the degradation kinetics. Not surprisingly, transmittance modulation of ECD3 optical modulation is degraded from ~60% in initial cycles to ~30% around 160 cycles in such a cycling mode (Fig. 2d). Derived from its inability to bleach, the bleached transmittance is significantly lowered while the transmittance in the colored state continues its decrease except for a very low scan rate of 1 mV s^{-1}. Here, the bleaching failure should account for ECD3 fast degradation. In this case, both the bleached and colored transmittances decrease upon cycling, showing a downward trend overall. Contrary to the degradation behavior of ECD2, this decay form with the transmittance curve decreasing as a whole is defined as ''downtrend degradation''. As we know, for cathodic coloring WO_3, Li^+ insertion with compensating electrons is accompanied by the coloring process (transmittance decrease). Conversely, for anodic NiO, cation incorporation together with electrons will favor bleaching (transmittance increase). In our work, in general, ECD3 demonstrates a downward trend in the transmittance evolution. It can be reckoned reasonably that cation trapping in WO_3 is responsible for the transmittance decrease of ECD3.

To further explain this phenomenon, Q as well as CE is evaluated (Fig. 2e). A significant increase in device capacity associated with a decrease in color efficiency with a scan rate decrease is observed. The value of Q is as high as 250 C m^{-2} when the scan rate decreases to 1 mV s^{-1}, while the CE decreases to less than 40 cm^2 C^{-1}, suggesting a significant decrease in the ability to arouse color change for a specific charge. Obviously, the large charge capacity cannot account for the ECD3 optical contrast shrinkage, so the declination can only be ascribed to the poor efficiency of these charges. As more and more Li^+ ions are inserted/extracted during slow scans, the ''site saturation'' is a suitable explanation to the efficiency decrease. Further studies are needed to confirm this deduction. In addition, as far as we are concerned, the micro-structure evolution (as demonstrated in Fig. 8) may also contribute to the coloration efficiency. The harsh electrochemical cycling has caused a highly dense structure. The structural congestion occurred in the film will prevent ions from penetrating through the network freely and cut part of their diffusion paths, thus keeping these ions from arousing color change efficiently. On the basis of the electrochemical analysis, the accelerated cycling mode results in different degradation mechanisms in ECD3 from conventionally long-term cycled ECD2.

In order to allow structural and compositional measurements for subsequent investigation of the degradation mechanism within the cathodic and anodic EC layers after cycling, the full devices were disassembled gently step by step. The sealer is firstly cleaned using a dispersant. The single layers on the glass substrate can be easily separated after removing the spacers. The remaining gel polymer electrolytes on the separated single layers need to be removed using diluted acetone and alcohol before further characterizations and measurements.

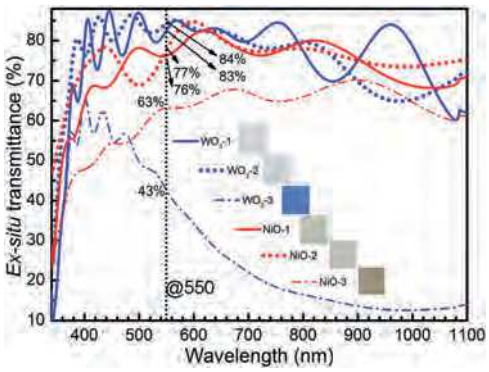

Fig. 3 Spectral transmittance for the disassembled non-cycled and cycled cathodic (WO_3-1 and WO_3-2, WO_3-3 respectively) and anodic EC (NiO-1 and NiO-2, NiO-3 respectively) films. Insets are the corresponding photographs of the films.

Ex situ measurements of optical properties are performed on cathodic (WO_3 on ITO) and anodic EC (NiO on ITO) layers in the $350 < \lambda < 1100$ nm range and the real pictures are insets for comparison (Fig. 3). After the electrochemical insertion and extraction of lithium cations, ideally, the films should return to their initial transparency. However, some of them retain their colored state to some degree, a sign of an irreversible coloring phenomenon. Here, it is really necessary to mention the concept of optical memory effect in the studies of *ex situ* transmittance. As a key criterion, the memory effect is defined as the ability to maintain the transmittance value of the electrochromic layer or the device after the potential is removed. Due to the finite electron-blocking capacity of the ion electrolyte layer and the weak interfacial energy between the ion electrolyte layer and electrochromic layers, typically a five-layer all-solid-state device generally suffers from poor optical memory. In our work, the device does not show a good memory effect, associated with an obvious self-erasing process taking place in the device under open-circuit conditions. Our research group has reported[28] the self-erasing phenomenon of a typical five-layer device and has made comparison with a seven-layer device embedded with buffer layers. Under open-circuit conditions, it just takes less than 100 s for the typical five-layer device in the colored state to spontaneously bleach. This means, after we remove the potential for *ex situ* T% measurements, the device will get less and less colored to be in the near bleaching state in minutes.

For better comparison, the detailed transmittance values extracted from the figures above are summarized in Table 3. The specific values of the initial and final *in situ* transmittance of ECD2 and ECD3 at 550 nm as well as the *ex situ* transmittance of disassembled relevant films are listed in the table. Final colored *in-situ* transmittance of ECD3 (values represented in boldface) is as low as 12%, but the *ex situ* transmittance of disassembled WO_3-3 and NiO-3 is much higher, up to 43% and 63%. A ''transmittance discrepancy'' problem does occur in both ECD2 and ECD3. Then, what has caused the ''transmittance discrepancy'' problem? Can it be avoided? The typical five-layer ECD in our work will become more transparent after

Table 3 Transmittance of the ECD and relevant films at 550 nm

T% @ 550 nm		ECD2			ECD3			WO_3-1	NiO-1	WO_3-2	NiO-2	WO_3-3	NiO-3
		T_b	T_c	ΔT	T_b	T_c	ΔT						
In situ T%	Initial	78	24	54	78	11	67	—	—	—	—	—	—
	Final	65	*55*	10	53	**12**	41	—	—	—	—	—	—
Ex situ T%		—	—	—	—	—	—	83	76	*84*	*77*	**43**	**63**

an obvious self-erasing process taking place in the device under open-circuit conditions due to the poor optical memory effect. This can explain why there is "transmittance discrepancy" between *in situ* and *ex situ* transmittance values at 550 nm in ECD2 and ECD3, namely, final *in situ* 55% for ECD2 while *ex situ* 84% and 77% for WO_3-2 and NiO-2, and 12% for ECD3 while 43% and 63% for WO_3-3 and NiO-3. Furthermore, for the long-term gently-cycled ECD2 at fast scan rates, the device still retains good reversibility of transmittance circulation in the last few cycles. The *ex situ* transmittance of relevant WO_3-2 and NiO-2 is 84% and 77%, respectively. The total transmittance can be estimated by multiplying the two films' transmittance.

$$84\% \times 77\% \approx 65\%$$

The value of 65% is exactly the bleached transmittance of ECD2 at the final cycle 11 270. This provides powerful proof that films in ECD2 return to its fully-bleached state after the self-erasing process under the open-circuit condition.

For the accelerated harsh-cycled ECD3, good reversibility of transmittance circulation is not maintained till the end. The *ex situ* transmittance of WO_3-3 and NiO-3 is 43% and 63%, respectively. We cannot get the expected ECD3-bleached transmittance of 53% by multiplying due to its poor reversibility. That is, films in ECD3 will get less colored after potential removal but could not be fully bleached like ECD2. One more point we will mention is related to the washing of the gel polymer, removal of one layer will be sure to help increase the overall transparency, but the visible transmittance increase of the films mainly arises from the self-erasing effect of ECD2 and ECD3. Indeed, it will be perfect if the series of characterizations and measurements can be carried out by *in situ* methods on the films within the device. However, we also need to be aware of the fact that *in situ* testings are full of challenges and cannot be realized at present. Thereby, some compromise on the studies of the electrochromic film and the device degradation mechanism with the application of *ex situ* testings after the removal of potentials will be required.

The WO_3-3 and NiO-3 films from ECD3 that is harshly cycled at a slow scan rate exhibit a significantly decreased transmittance. This accelerated degradation arises from bleaching inability, according to what has been reported by R. T. Wen on film attenuation in a short period of time.[27] Contrarily, the WO_3-2 and NiO-2 films from ECD2 that is cycled constantly at 100 mV s^{-1} for 21 316 times, beyond expectation, show a comparable transparency with non-cycled films, but without any doubt they are different films intrinsically considering the variation or the shift of the crest and the trough of the transmittance curves.[29] The evolution mechanism from initial to degraded films, as well as the discordance resulting from two voltammetric cycling modes, as we will discuss below, might be associated with the Li trapping quantity and the trapping positions.

3.2 Structural/microstructure analysis of device degradation

The GIXRD patterns of the disassembled non-cycled (NiO-1) and cycled anodic (NiO-2 and NiO-3) EC films are presented in Fig. 4. No diffraction peaks are found in all disassembled non-cycled (WO_3-1) and cycled cathodic (WO_3-2 and WO_3-3) EC layers, suggesting the amorphous feature of all these films (Fig. S2, ESI†). In contrast, NiO films show a polycrystalline NaCl-type structure with a (111) preferred orientation.[30] The characteristic Bragg's peaks of the cubic structure NiO indexed as (111), (200), (220) and (311) notably exhibits a lower diffraction intensity for cycled NiO-2, as indicated by yellow arrows in Fig. 4, which implies that the crystallinity of the films tends to be weakened in the ECD2 life-time cycling process. No additional diffraction peaks representing other phases such as Ni_2O_3 or $LiNiO_2$ or any other compounds appear for cycled films.

In the Raman spectra (Fig. 5a), WO_3-3 possesses a broad peak different from those of the other two samples in the low wavelength region (100–500 cm^{-1}). The shoulder located at around 450 cm^{-1} is attributed to W^{5+}═O double bonds, formed by reduction of W^{6+}═O as electrons and balanced Li ions are inserted in the EC process.[31] The peak broadening of WO_3-3 in the range from 700 to 1000 cm^{-1} also gives some signs of the presence of mixed valencies. In addition, there is a broad peak at 240 cm^{-1} ascribed to W^{5+}–O bonding. This implies that the WO_3-3 contains W cations at different states (W^{5+} and W^{6+}) which can be only due to the Li insertion.[32] Upon Li^+ insertion,

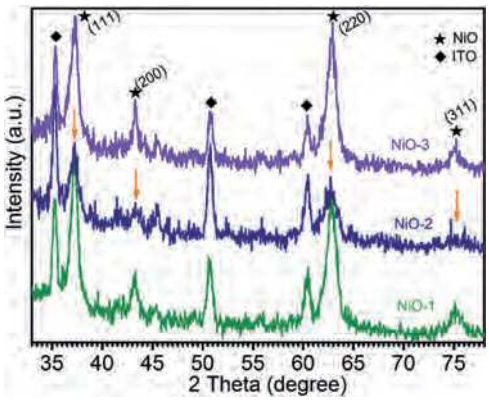

Fig. 4 GIXRD patterns of the disassembled non-cycled (NiO-1) and cycled anodic (NiO-2 and NiO-3) EC films.

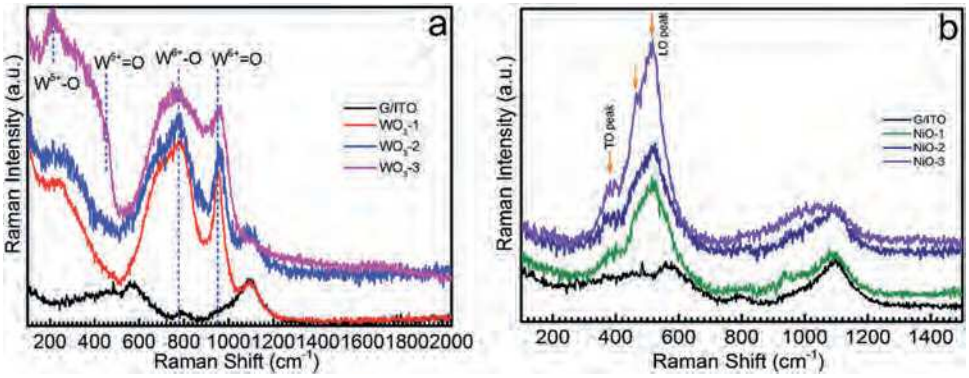

Fig. 5 Raman spectra of disassembled non-cycled and cycled (a) cathodic (WO_3-1 and WO_3-2, WO_3-3 respectively) and (b) anodic EC (NiO-1 and NiO-2, NiO-3, respectively) films.

in the low wavelength region, Li^+ cations normally induce the appearance of distinct peaks at around 200 cm^{-1}, arising from the stretching and bending vibrations of O–W–O bonding in Li_xWO_3 films.[32,33] Interestingly, in our system the W^{6+}═O bands remain unchanged upon Li insertion. Moreover, no peaks attributed to Li–O appear in the spectra, even though it has been already proposed that the cations affect network's vibrations[34] instead of residing only within the lattice channels. Bueno *et al.*[35] support that a high amount of Li intercalation may lead to a weak interaction W^{5+}–O ← Li between the lithium ions and the network, immobilizing the ions inside the films, although the Li–O bond is not detectable by Raman spectroscopy. For WO_3-3, the broadened peak in the low wavelength region (100–400 cm^{-1}) derives from W^{5+} (Li_xWO_3). Evidently, a fraction of cations reside inside the channels of the WO_6 octahedra. We believe that the permanent coloration or bleaching inability of WO_3-3 stems from the formation of stable Li_xWO_3. Besides, the Raman spectra of all the disassembled non-cycled and cycled cathodic (WO_3-1 and WO_3-2, WO_3-3 respectively) EC films show a broad and multi-component peak (500–850 cm^{-1}) due to the stretching vibrations of bridging W^{6+}–O and terminal W^{6+}.[35] A relatively sharp peak at 950 cm^{-1} is assigned to the stretching mode of the W^{6+}═O double bonds involving terminal oxygen atoms on the surface of clusters and microvoid structures in the film. The broadness of the peaks and the presence of W═O bonds are absent in crystalline materials,[36] indicating mainly the amorphous nature of the non-cycled films and the multi-cycled films.

The Raman spectra of all the disassembled non-cycled and cycled anodic (NiO-1 and NiO-2, NiO-3 respectively) EC films (Fig. 5b) in the 100–1500 wavenumber range show the characteristic peaks of the NiO phase.[37,38] First-order Transverse Optical (TO) and Longitudinal Optical (LO) phonon modes are located at 400 and 520 cm^{-1} respectively. Besides, NiO-3 presents also an additional peak that can be attributed to the non-stoichiometry. This peak is often described as a shoulder located in the left of the LO peak.[39,40] In our case, this extra peak is clearly shown in the spectra at 480 cm^{-1}. Mironova-Ulmane *et al.*[41] explained the activation of the peak at 450 cm^{-1} by the magnetostriction effect responsible for a rhombohedral distortion in NiO.

Fig. 6 shows the correlation of the degree of degradation with the microstructure of the surface of disassembled non-cycled and cycled cathodic (WO3-1 and WO3-2, WO3-3 respectively) and anodic EC (NiO-1 and NiO-2, NiO-3 respectively) films, as observed by AFM over an area of 1 × 1 μm^2 as well as SEM images (Fig. S3 and S4, ESI†). All the cycled films display decreased surface roughness (R) values, with altered surface morphologies most probably resulting from the repetitive insertion/extraction of Li^+ ions and their partial trapping effects. Furthermore, it is clearly demonstrated for WO_3-3 with a very dense and flat morphology totally different from non-cycled WO_3-1 that this micro change is closely associated with the irreversible coloring in WO_3-3. It is evident that the accelerated harsh voltammetric cycling mode leads to deterioration of the WO_3-3 films' morphology. In contrast, for WO_3-2, from ECD2 after conventional long-term voltammetric cycling, a less porous morphology with even smaller particles than WO_3-1 is presented. Thus, AFM reveals that two cycling modes will give two different micro evolutions in WO_3 films. Concerning the anodic EC layers, NiO-1 displays unambiguous grains distributed uniformly on the surface, but after extreme long-term cycling, the grain distribution in the NiO-2 micrograph becomes more uneven, which means they tend to be clustered in certain areas. For NiO-3, the harsh electrochemical cycling also results in the appearance of grain clusters as marked in the figure.

For subsequent cross-sectional SEM imaging of the disassembled uncycled and cycled WO_3 and NiO based films without any mechanical stress and/or contaminants like grinding/polishing slurries, FIB milling is used (Fig. 7 and 8). A 1.2 μm layer of Pt is coated on the top to prevent damage from FIB milling and a lamella is produced. From the FIB cut, typical elemental mappings confirm that the deposited films, namely, WO_3, NiO, and ITO, are present layer by layer on the glass and perfectly in the expected locations. In all the disassembled uncycled NiO-1 and cycled NiO-2 and NiO-3 EC layers, NiO films are found to have a porous framework comprised of small grains while WO_3 and ITO films exhibit a highly dense structure. Obviously, the microstructure of NiO is significantly affected by the voltammetric cycling protocols. In comparison

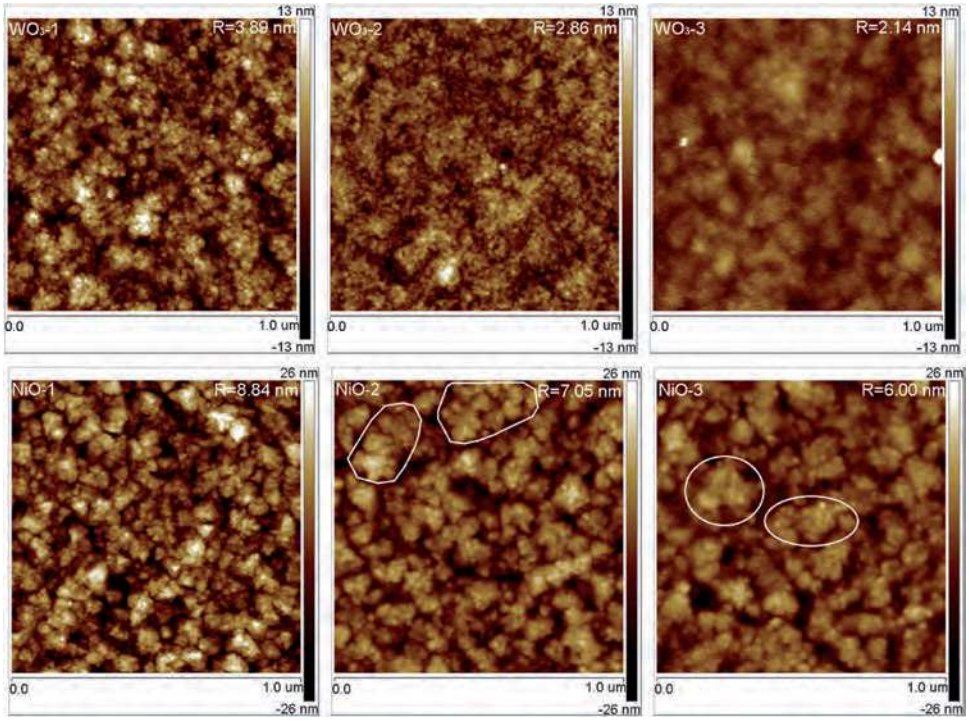

Fig. 6 AFM images of disassembled non-cycled and cycled cathodic (WO_3-1 and WO_3-2, WO_3-3 respectively) and anodic EC (NiO-1 and NiO-2, NiO-3 respectively) films (roughness values are shown; agglomeration evolution in degraded films is marked with white cycles).

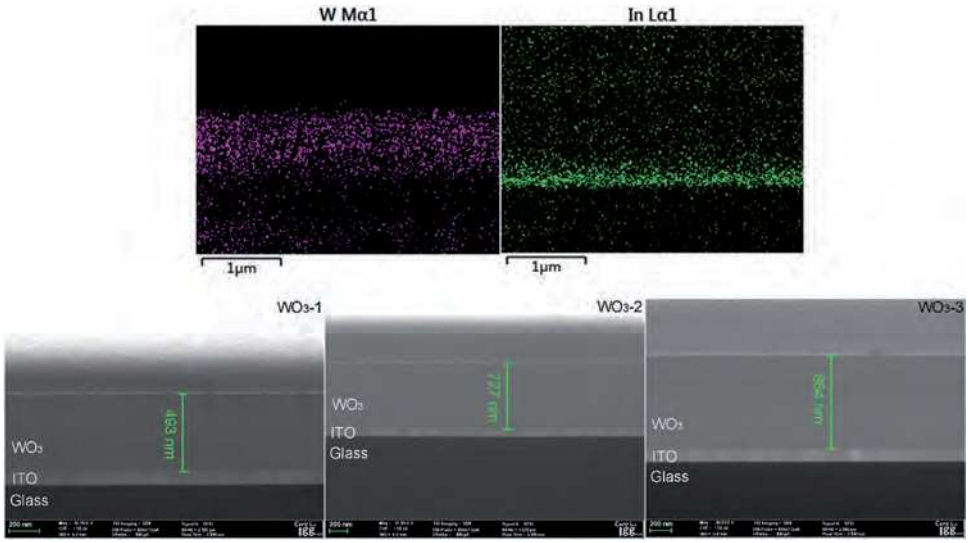

Fig. 7 Typical cross-view EDS-elemental mapping and SEM image of the FIB-cut sample for disassembled cathodic WO_3 EC films.

with uncycled NiO-1 and harsh-accelerated-cycled NiO-3, the porosity and empty volumes decrease to a great degree, creating a more smooth and dense morphology for degraded NiO-3. The structural congestion occurred in the film will prevent ions from penetrating through the network freely and cut part of their diffusion paths, thus depressing the charge capacity. However, it is an apparently different situation for extremely long-term cycled NiO-2. After continuous electrochemical cycling for as long as 426.32 hours, multiple repeated ion injections/extractions have resulted in the appearance of grain distortions and disordered network chains. Thereby, different voltammetric cycling procedures (scan rate; cycling time) will bring about different film morphological evolutions, which increases the complexity in the ECD degradation mechanism.

In addition, we have measured the film thickness in the figures and found that the WO_3-1, WO_3-2 and WO_3-3 film thicknesses are 493 nm, 727 nm and 864 nm, respectively, and NiO-1, NiO-2 and NiO-3 correspond to 380 nm, 520 nm and 680 nm,

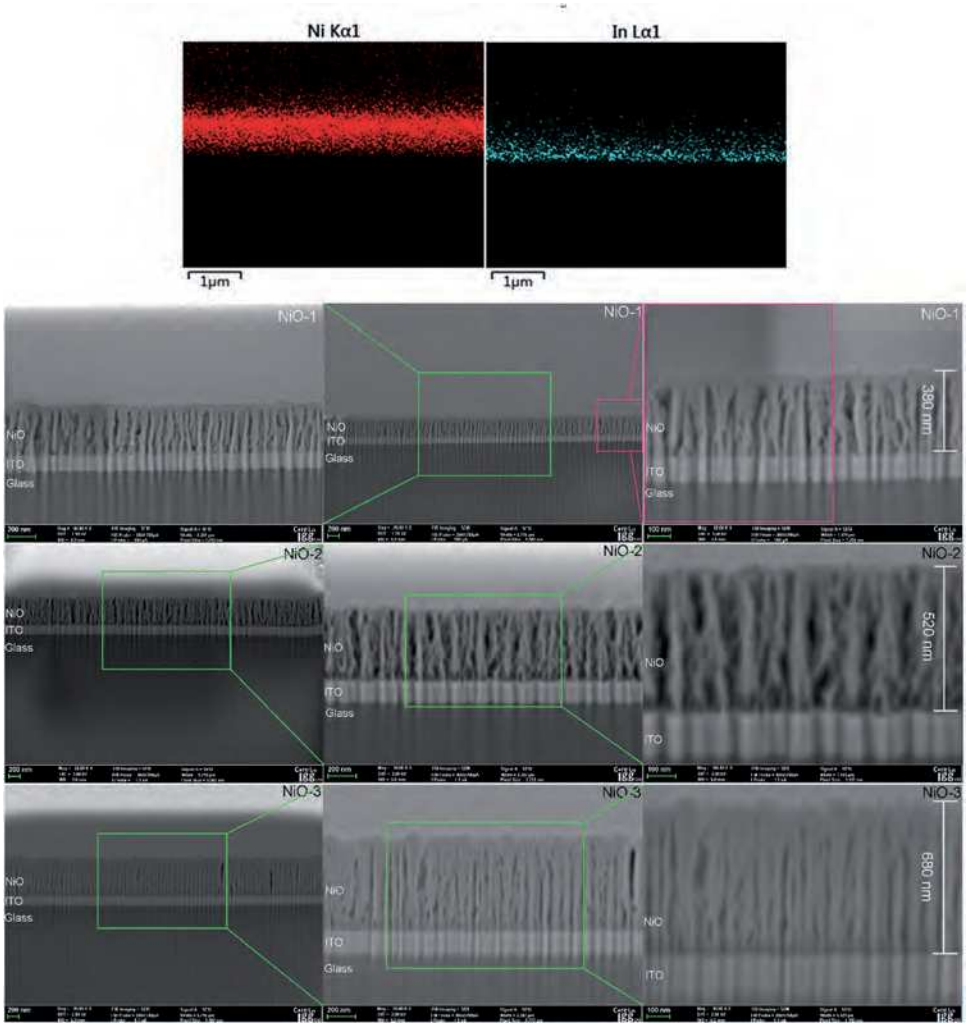

Fig. 8 Typical cross-view EDS-elemental mapping and SEM low/high magnification images of the FIB-cut samples for disassembled anodic NiO EC films (details are provided in the enlarged zoomed inset for better observation).

respectively (in Fig. 8). This unambiguously demonstrates that all the degraded films in the device, for both WO_3 and NiO, show a significant thickness increase, which is closely associated with the Li trapping (see discussions below in the SIMS section). Furthermore, it has been clearly demonstrated for electrochromic films with thickness above 100 nm and an insertion level corresponding to a Li-to-W ratio of 0.4 that the volume can grow by as much as $\sim$10% due to lithium insertion.[27,42] In our work, for the NiO films from severely degraded devices, significant lithium trapping is detected by the SIMS technique, and thus, the increase in thickness observed in the FIB-cut images is reasonable. In detail, the thickness increase of 36% for NiO-2 and of 79% for NiO-3 suggests that the trapped lithium ions are not at the same type of sites, in the case of conventional long-term and harsh accelerated voltammetric cycled devices. It must be stressed again that the microstructures shown by the FIB-cut are also different in NiO-2 and NiO-3, which once again confirms that the two cycling protocols affect the declining process separately. And the films' transmittance and color appear to be totally different (Fig. 3); the study of the impact of the degradation procedure on the film properties over time is thus clearly of interest.

3.3 Elemental analysis of device degradation

SIMS results can provide powerful evidence of the existence of different elements including Li within the films, but quantification is very challenging due to matrix and charging effects and is only possible with the use of standards (in order to define the Relative Sensitivity Factor RSF), which provides the conversion from the measured SIMS intensities (as seen in the *y*-axis) to the real impurity density (atom per cm^3).[43] Based on this, it makes no sense to compare the SIMS intensities of W (or Ni) with Li without their RSF values. In our case, the SIMS intensities of W and Li are shown in Fig. 9a and b respectively for disassembled non-cycled and cycled cathodic (WO_3-1 and WO_3-2, WO_3-3 respectively) WO_3 films. The absolute impurity density as well as the RSF is not provided but the relative intensities of each element could be compared as their matrix and charging effects are supposed to be identical in WO_3 films in our work. Fig. 9a clearly shows that the SIMS intensities of W

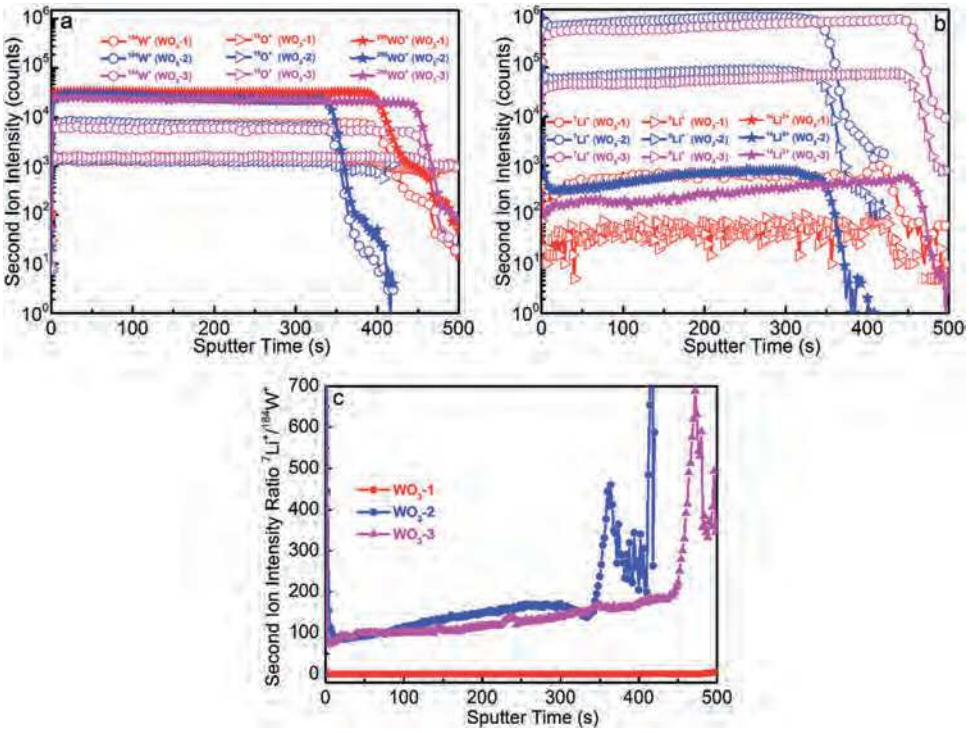

Fig. 9 SIMS data showing the second-ion-intensity level of (a) element W and (b) Li; (c) normalized intensity of Li for disassembled non-cycled and cycled cathodic (WO_3-1 and WO_3-2, WO_3-3 respectively) films. The W-complex signals from all the three films overlap to a high degree in panel a. The sharp decrease/increase in panel c indicates the WO_3/ITO interface.

are equivalent whatever be the films. The relative intensities of different Li signals ($^7Li^+$, $^6Li^+$, and $^{14}Li^{2+}$) are recorded. Fig. 9a clearly shows that W SIMS intensities are in great agreement, and based on this, the profiles corresponding to the $^7Li^+/^{184}W^+$ intensity ratios are presented (Fig. 9c) and discussed (the $^{184}W^+$ positive ion was taken as the reference signal). This data presentation, namely, calculated intensity ratio, enhances the visibility of the in-depth distribution of Li inside the oxide films.[44–46] Not surprisingly, the WO_3-1 film from ECD1 without any cycling shows almost no Li. However, the degraded WO_3-2 and WO_3-3 films are shown to possess a comparable Li trapping level, with the second ion ratio of $^7Li^+/^{184}W^+$ being near 100 and, most importantly, both films degraded in different cycling modes demonstrating a consistent Li concentration. The Li trapping process is evidenced in either conventional or harsh voltammetric cycling. Furthermore, the coincidence that the trapping Li content of WO_3-2 is in agreement with Li content of WO_3-3 after a totally different cycling procedure may indicate that the trap sites are almost fully occupied in both of the two degraded films or, alternatively, that an increased level of trapping in the host structure leads to stronger electrostatic repulsion between Li ions and prevents subsequent trapping.[47] Accordingly, it can be reckoned that the Li trapping saturation does exist in films upon cycling, thereby limiting the increase of the amount of immobile ion residues. In addition, a clear trend in the trapped Li concentration along with depth is observed in degraded films, and noticeably, there is as a whole a steady increase prior to the sharp increase at the film interface (Fig. 9c). The sputtering time increases homogeneously within the film depth, so the turning point of the sputtering time represents the end of the EC film region. In the first 300 seconds, the normalized Li intensity of the film increases continuously as shown in Fig. 9c. It therefore appears that more residual Li ions in the films suffer from deep traps rather than shallow traps, represented by a longer sputter time and a shorter time in the SIMS measurement (Fig. 9c), respectively. Deeper the location is, more difficult it is for the successful extraction, thus more irreversible ions there are.

What is more interesting, WO_3-2 and WO_3-3 films exhibit totally different optical properties as shown in Fig. 3 (*e.g.* transmittance and color), for which the consistent Li trapping level cannot account. In this section, although we do not have direct proof, we can reasonably reckon that the trapped Li ions, in the case of disassembled cycled cathodic (WO_3-2, WO_3-3 respectively) films, are not at the same type of sites (*i.e.*, they have different positions within the film structure and different chemical bonding energies), thus explaining the transmittance change and color difference. To support this deduction, we have found related contexts in the literature. N. Krins and H. Zheng have reported[8,23] that the inserted Li cations could (i) reside in the structural channels created by the linkage of WO_6 building units or (ii) react with the host's bridging oxygens by breaking the network's W–O–W chains and creating new W═O bonds[48,49] as shown in the following schematic (in Fig. 10):

The former cation trapping not involved in redox reactions is believed to be more related to the transparency of WO_3-2,

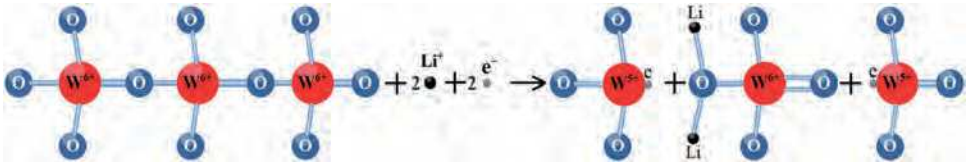

Fig. 10 Schematic of the reaction between lithium ions and WO_6 building units.

while the latter is associated with chemical reactions with the variation of valence states. The formation of stable W^{5+} ions is a perfect explanation to the blue color of WO_3-3. We can reckon that different positions of the residual cations will lead to different film optical properties. To provide powerful experimental evidence for this argument, XPS measurements will be carried out in the final part.

The SIMS analysis and research ideology used in EC cathodic WO_3 films are extended and applied to EC anodic NiO films. The Ni signals still remain constant in NiO-1, NiO-2 and NiO-3 (Fig. 11a). Interestedly, the Li signal intensities of different NiO films do not remain at the same level (Fig. 11b), as presented clearly in the normalized Li intensities (Fig. 11c) assessed by means of the $^{7}Li^{+}/^{158}Ni^{+}$ ratio. It is shown that about 3 times the amount of Li ions are trapped in disassembled cycled anodic NiO-2 than NiO-3 films, suggesting that long-time conventional voltammetric cycling at a fast scan rate will also lead to guest ion filling in the anodic NiO layer, but due to the lack of RSF definition, quantification cannot be realized to compare the trapped Li levels between NiO and WO_3. Noticeably, before the sharp increase of the normalized Li intensity, there is also a steady increase, indicative of the presence of a gradient in the Li concentration along film depth.

Finally, to investigate the effects of Li trapping on chemical bonding within W and Ni oxides, we carry out XPS analysis on disassembled non-cycled and cycled cathodic (WO_3-1 and WO_3-2, WO_3-3 respectively) and anodic EC (NiO-1 and NiO-2, NiO-3 respectively) films (Fig. 12 and Fig. S5, ESI†). Carbon is used as a calibration source in the XPS measurement. For comparison, the binding energies of all the samples are set by fixing the C 1s peak due to carbon contamination to 284.8 eV. W4 f spectra of the films consist of well-resolved spin orbit split double peaks corresponding to W $4f_{7/2}$ and $W4f_{5/2}$ states. For the non-cycled pure W oxide film the positions of the two peaks represent only a W^{6+} state, indicative of transparent WO_3. As compared to the case of transparent W oxide films from ECD2, the peak location shift towards a higher energy has been found, which has been double checked from repeated measurements. The binding energies of the two peaks are increased by about 1 eV. It is already known from SIMS analysis that more than 100 times of

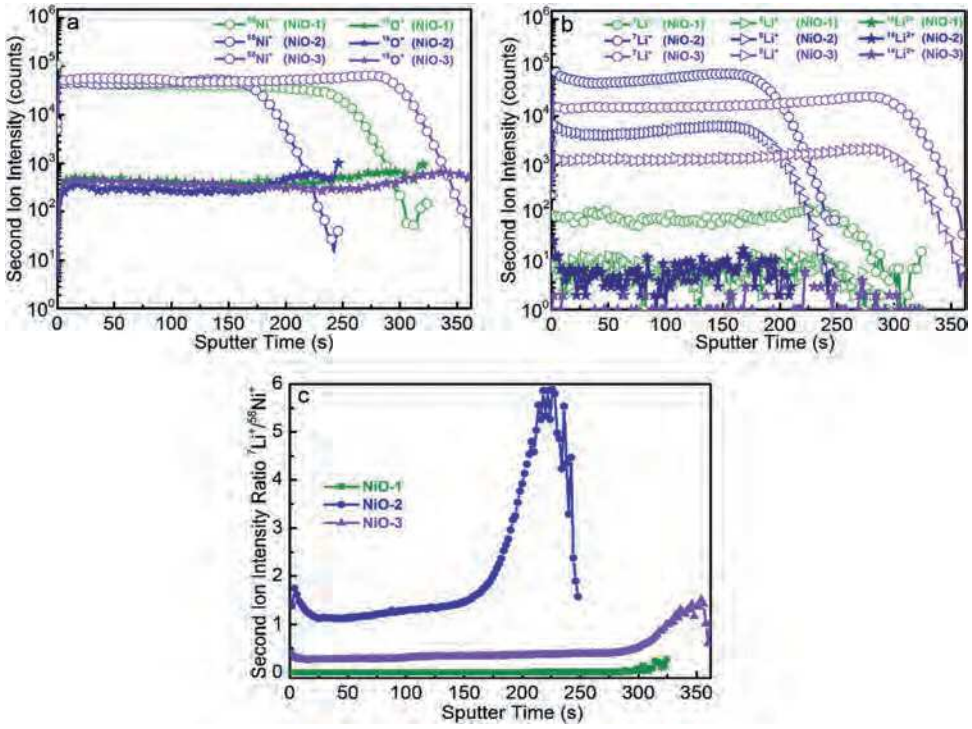

Fig. 11 SIMS data showing the second-ion-signal-intensity level of (a) element Ni and (b) Li; (c) normalized intensity of Li for disassembled non-cycled and cycled anodic (NiO-1 and NiO-2, NiO-3 respectively) films. The Ni-complex signals from all the three films overlap to a high degree in panel a. The sharp decrease/increase in panel c indicates the NiO/ITO interface.

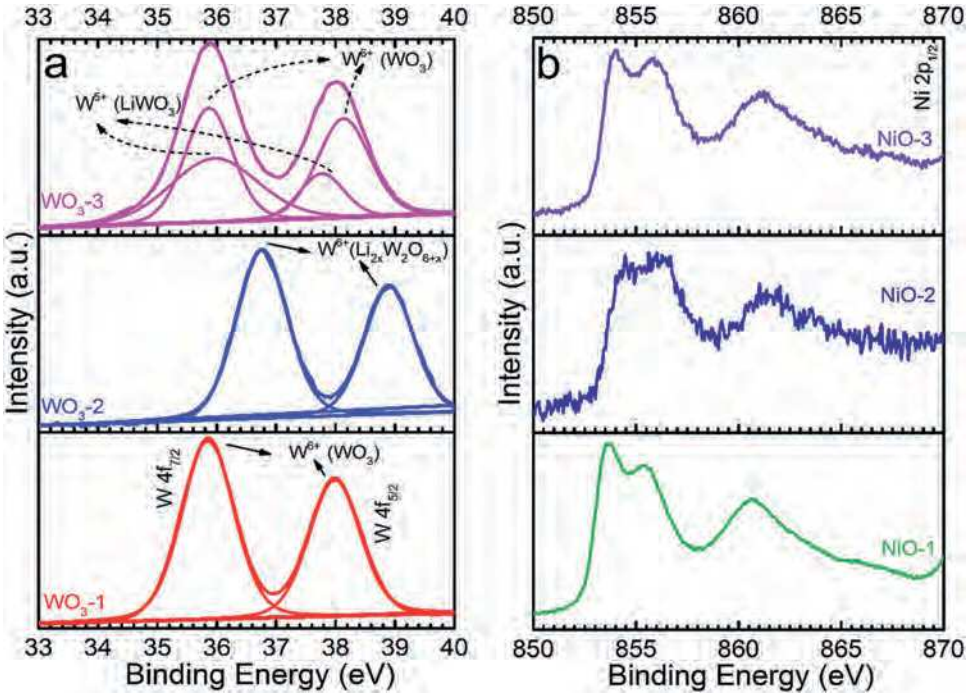

Fig. 12 XPS detail spectra for disassembled non-cycled and cycled (a) cathodic (WO_3-1 and WO_3-2, WO_3-3 respectively) and (b) anodic EC (NiO-1 and NiO-2, NiO-3 respectively) films.

Li exist in W oxides from ECD2 than the non-cycled pure WO_3-1, and the W–O distance has been reported to be substantially larger in the proton or Li^+ intercalated films.[10] Thus, it is believed that such a XPS peak shift arises from the large amount of Li trapping effects on the W–O binding energy. It is worth noting here that this trapping behavior does cause no forever coloring phenomenon (see Fig. 3). So the shifted peak does not belong to W^{5+} or W^{4+} (blue). Moreover, W^{5+} or W^{4+} corresponds to a lower energy rather than a higher energy direction.[50] As a result, the shifted two peaks again suggest a W^{6+} state, corresponding to transparent compounds with the formula $Li_{2x}W_2O_{6+x}$ (x = 1, 2, 3...) after Li trapping. The amorphous feature of this compound as well as the complexity of the WO_3–Li_2O system[51] makes it very challenging to determine what the specific compound (the value of x) is or if it is a mixture of several compounds.

For the W oxide from ECD3, some peak broadening is observed due to the presence of tungsten ions W^{5+} after Li trapping.[52] From XPS overlapping peak resolving analysis, the ratio of W^{5+}/W^{6+} can be evaluated to be 42/58. The existence of reduced W^{5+} ions ($LiWO_3$) with blue color gives a good explanation on the irreversible coloring state of the films. For Ni oxides the Ni 2p spectra contain multiple peaks at binding energies between 850 and 870 eV, including the main peak and satellites. The Ni 2p spectra are often complex and it is difficult to assign specific binding energies to Ni^{2+} and Ni^{3+} states.[53,54] There are two main bands closely associated with Ni^{2+} and Ni^{3+} located at 853 to 857 eV. Carley *et al.*[55] proposed the assignment of binding energies of 854.6 and 856.1 eV to Ni $2p_{3/2}$ XPS spectra for Ni^{2+} and Ni^{3+} respectively. More recent work from Biesinger *et al.* shows that the envelope spectra are better fitted by using multiplet splitting.[56] Due to peak asymmetries, complex multiplet splitting, shake-up and plasmon loss structure, and overlapping binding energies, it is quite difficult to determine the proportion of different valences. Moreover the possible presence of residual surface contaminant like hydroxide or oxyhydroxide species after soft surface cleaning by etching can lead to additional misinterpretations on the presence of Ni^{3+} in the NiO phase. So we will conduct only a qualitative comparison. The main peaks progressively shift towards higher binding energies for both of the two Ni oxides from degraded ECD2 and ECD3. The binding energy increase is believed to mainly result from the Li trapping fact evidenced by SIMS data. The brownish color of the Ni oxide film from ECD3 as well as the widening and shifting of its peak gives a sign of the presence of Ni^{3+} ions, and the transparency in NiO-2 is indicative of Ni^{2+}. In the degraded oxides with the existence of Li, the Ni^{2+} and Ni^{3+} may correspond to $Li_{2y}Ni_2O_{2+y}$ and $Li_{2z}Ni_2O_{3+y}$, respectively (where y, z can be 1, 2, 3...), though the specific compound is not decided. In addition, peak shapes and locations of the two decayed Ni oxides (from ECD2 and ECD3) are not completely identical, for which inconsistent Li trapping quantities and positions can account to a certain degree. H. Moulki *et al.*[57] have reported on the NiO based thin films by lithium addition and drawn conclusions that lithium addition remarkably deteriorates the preferred orientation and creates partial disorder, which can in general provide some references to our NiO:Li mixture regardless of the experimental detail difference. Here, the broadening of the main peak of the XPS Ni 2p spectra for NiO-2 may also arise from the disorder of the film structure. Repeated ion/electron insertion is thus accompanied by a distortion of the local structure,

which points to the effect of long-term electron–cation interactions in the device. In addition, after the Li trapping, some oxygen surrounding Ni elements will be dragged away from its original position in the lattice by guest Li, thereby weakening the Ni-O chemical bonds formed by the outermost electrons. The decrease of the outermost electron cloud density will strengthen the hold of inner electrons on their nucleus. Thereby, when more Li elements are trapped, a higher binding energy for Ni 2p is detected (Fig. 12b).

4 Conclusion

The present work demonstrated structural, compositional and surface chemical characterizations, allowing comprehensive assessments of the electrochromism mechanism in full devices subjected to charge capacity as well as optical degradations by (i) conventional life-time extensive voltammetry cycling and (ii) accelerated short-term harsh electrochemical cycling. In FIB-cut morphologies, it is demonstrated that the degraded films in the device show a significant thickness increase, which is associated with the Li incorporation as well as the microstructure deterioration. The SIMS results exhibited unambiguous ion-trapping evidence interpreting the charge density decline of the device. Indeed, the similar amount of Li cations trapped in degraded WO_3 films, whatever the cycling procedure was, is indicative of a trap saturation phenomenon. In combination with chemical binding energy analysis, the peak shift gave an implication of the different types of trapping positions, influenced by the cycling process, and the ions can only reside in the structural channels or even break the chemical bonding, thus resulting in significant physical change, mainly different colors and variable surface roughness. Additionally, SIMS measurements exhibited a clear upward trend in the trapped Li content along with depth. All our findings have provided a deep insight into the degradation of electrochromism in films as well as in full devices undergoing life-time or accelerated electrochemical cycling and, we trust, the valuable information will offer inspiration to the understanding of the mechanisms at play.

Conflicts of interest

There are no conflicts to declare.

Acknowledgements

This work was financially supported by the National Program on Key Research Project (2016YFB0303900) and the Academic Excellence Foundation of BUAA for PhD Students (2017062).

References

1 S. J. Yoo, J. W. Lim and Y. E. Sung, *Sol. Energy Mater. Sol. Cells*, 2006, **90**, 477–484.
2 C. G. Granqvist, *Handbook of Inorganic Electrochromic Materials*, Elsevier, 1995.
3 M. Fabretto, T. Vaithianathan, C. Hall, J. Mazurkiewicz, P. C. Innis, G. G. Wallace and P. Murphy, *Electrochim. Acta*, 2008, **53**, 2250–2257.
4 R. T. Wen, C. G. Granqvist and G. A. Niklasson, *ChemElectroChem*, 2016, **3**, 266–275.
5 C. G. Granqvist, *Thin Solid Films*, 2014, **564**, 1–38.
6 R. J. Mortimer, D. R. Rosseinsky and P. M. Monk, *Electrochromic Materials and Devices*, John Wiley & Sons, 2015.
7 O. Pyper, A. Kaschner and C. Thomsen, *Sol. Energy Mater. Sol. Cells*, 2002, **71**, 511–522.
8 H. Zheng, J. Z. Ou, M. S. Strano, R. B. Kaner, A. Mitchell and K. Kalantar-zadeh, *Adv. Funct. Mater.*, 2011, **21**, 2175–2196.
9 J. V. Gabrusenoks, P. D. Cikmach, A. R. Lusis, J. J. Kleperis and G. M. Ramans, *Solid State Ionics*, 1984, **14**, 25–30.
10 G. A. Niklasson and C. G. Granqvist, *J. Mater. Chem.*, 2007, **17**, 127–156.
11 D. Zhou, D. Xie, X. Xia, X. Wang, C. D. Gu and J. P. Tu, *Sci. China: Chem.*, 2017, **60**(1), 3–12.
12 J. H. Zhang, G. F. Cai, D. Zhou, H. Tang, X. L. Wang, C. D. Gu and J. P. Tu, *J. Mater. Chem. C*, 2014, **2**, 7013–7021.
13 G. F. Cai, J. P. Tu, D. Zhou, L. Li, J. H. Zhang, X. L. Wang and C. D. Gu, *CrystEngComm*, 2014, **16**, 6866–6872.
14 R. T. Wen, C. G. Granqvist and G. A. Niklasson, *Nat. Mater.*, 2015, **14**, 996–1002.
15 R. T. Wen, S. Malmgren, C. G. Granqvist and G. A. Niklasson, *ACS Appl. Mater. Interfaces*, 2017, **9**, 12872–12877.
16 D. M. Dong, W. W. Wang, G. B. Dong, Y. L. Zhou, Z. H. Wu, M. Wang, F. M. Liu and X. G. Diao, *Appl. Surf. Sci.*, 2015, **357**, 799–805.
17 D. M. Dong, W. W. Wang, G. B. Dong, Y. L. Zhou, Z. H. Wu, M. Wang, F. M. Liu and X. G. Diao, *Appl. Surf. Sci.*, 2016, **383**, 49–56.
18 D. M. Dong, W. W. Wang, G. B. Dong, F. Zhang, H. Yu, Y. C. He and X. G. Diao, *RSC Adv.*, 2016, **6**, 111148–111160.
19 D. M. Dong, W. W. Wang, A. Barnabé, L. Presmanes, A. Rougier, G. Dong, F. Zhang, H. Yu, Y. He and X. Diao, *Electrochim. Acta*, 2018, **263**, 277–285.
20 Q. Liu, G. Dong, Y. Xiao, M. P. Delplancke-Ogletree, F. Reniers and X. Diao, *Sol. Energy Mater. Sol. Cells*, 2016, **157**, 844–852.
21 P. R. Bueno, F. M. Pontes, E. R. Leite, L. O. S. Bulhões, P. S. Pizani, P. N. Lisboa-Filho and W. H. Schreiner, *J. Appl. Phys.*, 2004, **96**, 2102–2109.
22 F. Lin, D. Nordlund, T. C. Weng, R. G. Moore, D. T. Gillaspie, A. C. Dillon, R. M. Richards and C. Engtrakul, *ACS Appl. Mater. Interfaces*, 2013, **5**, 301–309.
23 A. G. Marrani, V. Novelli, S. Sheehan, D. P. Dowling and D. Dini, *ACS Appl. Mater. Interfaces*, 2014, **6**, 143–152.
24 X. Qi, G. Su, G. Bo, L. Cao and W. Liu, *Surf. Coat. Technol.*, 2015, **272**, 79–85.
25 H. Moulki, D. H. Park, B.-K. Min, H. Kwon, S.-J. Hwang, J.-H. Choy, T. Toupance, G. Campet and A. Rougier, *Electrochim. Acta*, 2012, **74**, 46–52.
26 R. T. Wen, M. A. Arvizu, M. Morales-Luna, C. G. Granqvist and G. A. Niklasson, *Chem. Mater.*, 2016, **28**, 4670–4676.

27 B. Baloukas, M. A. Arvizu, R. T. Wen, G. A. Niklasson, C. G. Granqvist, R. Vernhes, J. E. Klemberg-Sapieha and L. Martinu, *ACS Appl. Mater. Interfaces*, 2017, **9**, 16995–17001.

28 Q. R. Liu, G. B. Dong, Q. Q. Chen, J. J. Guo, Y. Xiao, M. P. Delplancke-Ogletree, F. Reniers and X. G. Diao, *Sol. Energy Mater. Sol. Cells*, 2018, **174**, 545–553.

29 M. A. Arvizu, R. T. Wen, D. Primetzhofer, J. E. Klemberg-Sapieha, L. Martinu, G. A. Niklasson and C. G. Granqvist, *ACS Appl. Mater. Interfaces*, 2015, **7**, 26387–26390.

30 M. Kitao, K. Izawa and K. Urabe, *Jpn. J. Appl. Phys.*, 1994, **33**(12), 6656.

31 K. Kim, C. Seo, H. Cheong and S. H. Lee, *J. Korean Phys. Soc.*, 2006, **48**, 1657–1660.

32 A. Baserga, V. Russo, F. D. Fonzo, A. Bailini, D. Cattaneo, C. S. Casari, A. L. Bassi and C. E. Bottani, *Thin Solid Films*, 2007, **515**, 6465–6469.

33 P. R. Bueno, F. M. Pontes, E. R. Leite, L. O. S. Bulhões, P. S. Pizani, P. N. Lisboa-Filho and W. H. Schreiner, *J. Appl. Phys.*, 2004, **96**, 2102–2109.

34 O. Pyper, A. Kaschner and C. Thomsen, *Sol. Energy Mater. Sol. Cells*, 2002, **71**, 511–522.

35 G. Leftheriotis, S. Papaefthimiou and P. Yianoulis, *Sol. Energy Mater. Sol. Cells*, 2004, **83**, 115–124.

36 D. Chatzikyriakou, N. Krins, B. Gilbert, P. Colson, J. Dewalque, J. Denayer, R. Cloots and C. Henrist, *Electrochim. Acta*, 2014, **137**, 75–82.

37 R. E. Dietz, G. I. Parisot and A. E. Meixner, *Phys. Rev. B: Condens. Matter Mater. Phys.*, 1971, **4**, 2302–2310.

38 J. C. Lai, X. C. Wang, W. B. Mi, Y. H. Ding and B. H. Yang, *Phys. Rev. B: Condens. Matter Mater. Phys.*, 2015, **478**, 89–94.

39 S. H. Lee, H. M. Cheong, N. G. Park, C. E. Tracy, A. Mascarenhas, D. K. Benson and S. K. Deb, *Solid State Ionics*, 2001, **140**, 135–139.

40 M. Wang, Y. Thimont, L. Presmanes, X. Diao and A. Barnabe, *Appl. Surf. Sci.*, 2017, **419**, 795–801.

41 N. Mironova-Ulmane, A. Kuzmin, I. Steins, J. Grabis, I. Sildos and M. Pars, *J. Phys.: Conf. Ser.*, 2007, **93**, 012039.

42 G. Garcia-Belmonte, J. Garcia-Cañadas and J. Bisquert, *J. Phys. Chem. B*, 2006, **110**, 4514–4518.

43 R. G. Wilson, F. A. Stevie and C. W. Magee, *Secondary Ion Mass Spectrometry: A Practical Handbook for Depth Profiling and Bulk Impurity Analysis*, Wiley, 1989, p. 384.

44 F. Decker, F. Donsanti, A. Salvi Maria, N. Ibris, J. E. Castle, F. Martin, D. Alamarguy, A. Vuk Surca, B. Orel and A. Lourenco, *J. Braz. Chem. Soc.*, 2008, **19**, 667–671.

45 J. Swiatowska-Mrowiecka, F. Martin, V. Maurice, S. Zanna, L. Klein, J. Castle and P. Marcus, *Electrochim. Acta*, 2008, **53**, 4257–4266.

46 J. E. Castle, F. Decker, A. Salvi Maria, F. A. Martin, F. Donsanti, N. Ibris and D. Alamarguy, *Surf. Interface Anal.*, 2008, **40**, 746–750.

47 R. T. Wen, M. A. Arvizu, M. Morales-Luna, C. G. Granqvist and G. A. Niklasson, *Chem. Mater.*, 2016, **28**, 4670–4676.

48 G. Leftheriotis, S. Papaefthimiou and P. Yianoulis, *Sol. Energy Mater. Sol. Cells*, 2004, **83**, 115–124.

49 J. G. Zhang, D. K. Benson, C. E. Tracy, S. K. Deb, A. W. Czanderna and C. Bechinger, *J. Electrochem. Soc.*, 1997, **144**, 2022–2026.

50 S. V. Green, A. Kuzmin, J. Purans, C. G. Granqvist and G. A. Niklasson, *Thin Solid Films*, 2011, **519**, 2062–2066.

51 P. Tabero and A. Frackowiak, *J. Therm. Anal. Calorim.*, 2017, **130**, 311–318.

52 J. Zhang, J. P. Tu, X. H. Xia, Y. Qiao and Y. Lu, *Sol. Energy Mater. Sol. Cells*, 2009, **93**, 1840–1845.

53 A. P. Grosvenor, M. C. Biesinger, R. S. C. Smart and N. S. McIntyre, *Surf. Sci.*, 2006, **600**, 1771–1779.

54 E. Avendaño, H. Rensmo, A. Azens, A. Sandell, G. D. M. Azevedo, H. Siegbahn, G. A. Niklasson and C. G. Granqvist, *J. Electrochem. Soc.*, 2009, **156**, 132–138.

55 A. F. Carley, S. D. Jackson, J. N. O'Shea and M. W. Roberts, *Surf. Sci.*, 1999, **440**, L868–L874.

56 M. C. Biesinger, B. P. Payne, L. W. M. Lau, A. Gerson and R. S. C. Smart, *Surf. Interface Anal.*, 2009, **41**, 324–332.

57 H. Moulki, D. H. Park, B. K. Min, H. Kwon, S. J. Hwang, J. H. Choy, T. Toupance, G. Campet and A. Rougier, *Electrochim. Acta*, 2012, **74**, 46–52.

Supporting Information

Lithium trapping as degradation mechanism of electrochromic properties of WO_3//NiO device

Dongmei Dong, Wenwen Wang, Aline Rougier, Guobo Dong, Fan Zhang, Hang Yu, Yingchun He, Xungang Diao, Antoine Barnabé*

Contents of Supporting Information

1. Design of electrochromic device

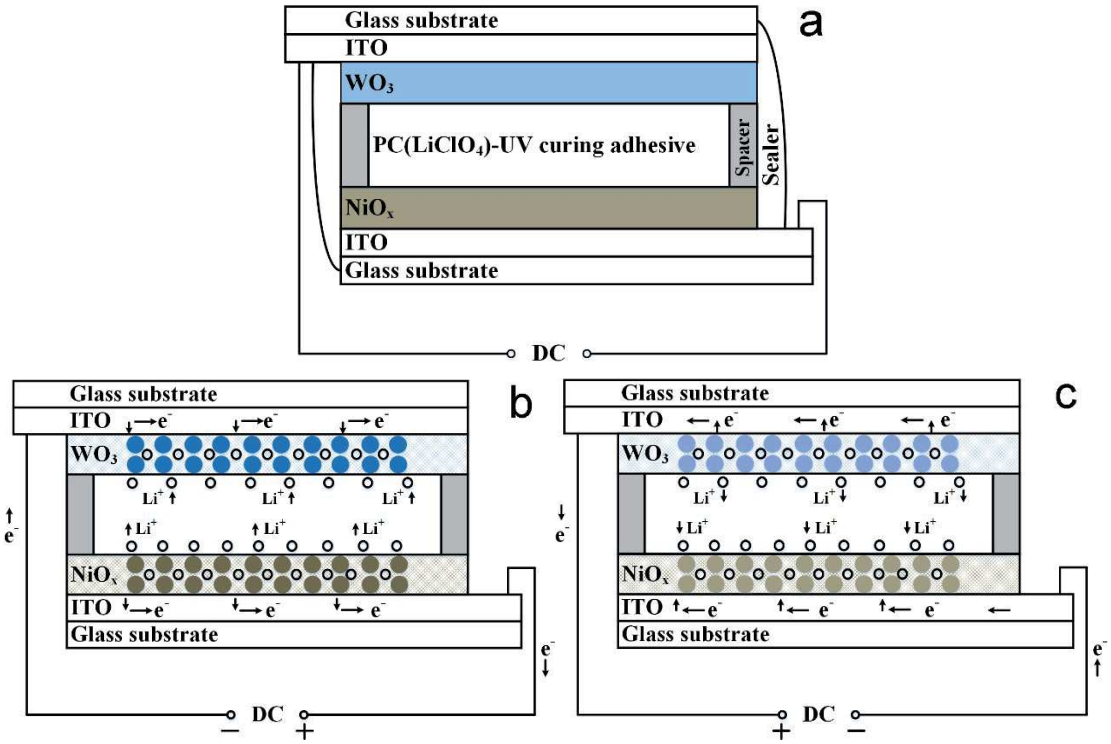

Fig. S1 Schematic cross-sectional view of design and working principle of the full laminated ECD: ITO/WO3/$LiClO_4$(PC)-UV curing adhesive/NiO/ITO at (a) as-deposited, (b) coloring and (c) bleaching states.

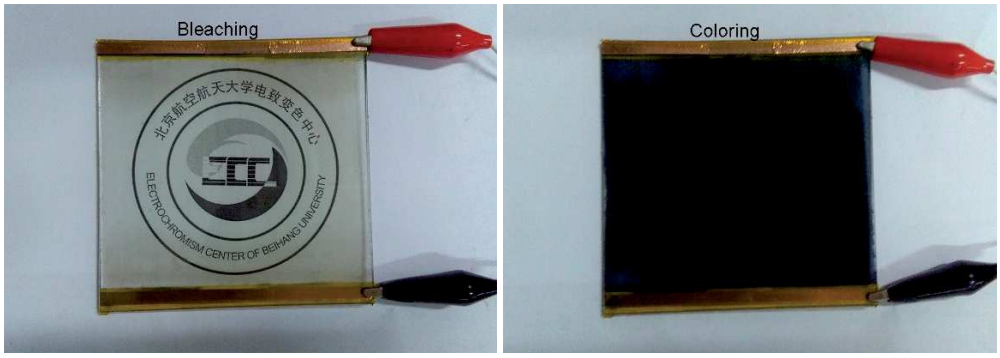

Fig. S2 Pictures of the full electrochromic device at bleaching and colored states.

As depicted in Fig. S1(a), the ECD consists of a cathodic EC layer WO_3 on transparent electrode ITO, an anodic EC layer NiO on ITO, and between them a gel polymer electrolyte containing Li cations and anions. It is widely accepted the EC effect involves the simultaneous insertion/extraction of electrons provided by an external potential and Li cations from gel polymer electrolyte (GPE) and the subsequent formation of coloring centers W^{5+} and Ni^{3+} or bleaching W^{6+} and Ni^{2+}.[1] Fig. S1(b) & (c) demonstrates the diagram of the coloring and bleaching process of the device,

respectively. The cathodic W oxide film, which has high transparency in the oxidized state W^{6+} and exhibits blue color when it is reduced to W^{5+} by electron insertion together with Li^+, or vice versa, and the anodic Ni oxide film, which has opposite electrochromism to the former, or turns to be brownish in Ni^{3+} states accompanying the extraction of electrons and Li^+. The digital pictures of the full electrochromic device at bleaching and colored states are presented in Fig. S2.

2. Structural characterization of degraded films

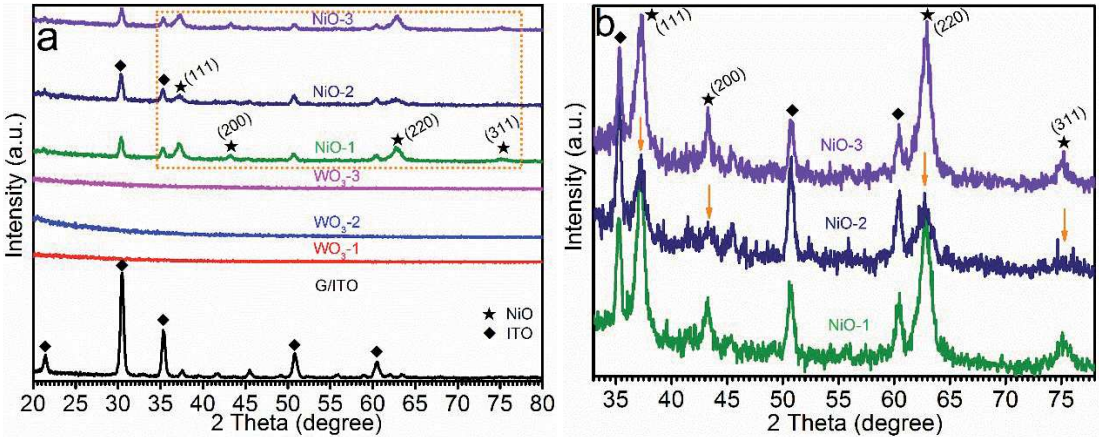

Fig. S3 (a) XRD patterns of the non-cycled and cycled films from as-prepared and degraded ECDs; (b) Partial enlarged drawing of rectangular region indicated by the yellow dashed line.

The XRD patterns of the films from degraded devices are presented in Fig. S3. A small incidence angel ω of 0.3 degree is used to avoid the strong signal intensity of ITO. No diffraction peaks are found in all WO_3 films, suggesting the amorphous feature of non-cycled WO_3-1 as well as cycled WO_3-2 and WO_3-3. Conversely, NiO films show a polystalline NaCl-type structure indexed as (111), (200), (220) and (311) crystal planes recide by a noticable extent for cycled NiO-2, as indicated by the yellow arrows, which implies the crystallinity of the films tends to be weakened in ECD2 life-time cycling process. Moreover, no additional diffraction peaks representing other phases such as Ni_2O_3 or $LiNiO_2$ or any other compounds appear for cycled films. As described in Kitao et al.,[2] the Ni^{3+} ions are performed as color centers in films. Thus, the brownish samples contain not only Ni^{2+} ions but also a certain amount of Ni^{3+} ions, and they exists in amorphous state.

3. Surface characterization of degraded films

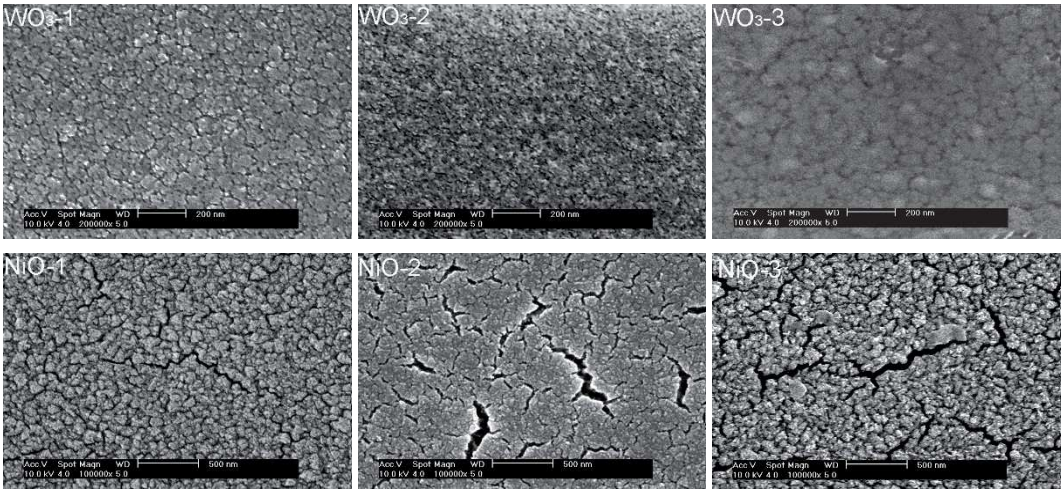

Fig. S4 SEM images for WO_3 and NiO films.

In Fig. S4 & S5, it is clearly demonstrated for WO_3-3 with a very dense and flat morphology totally different from non-cycled WO_3-1 that this micro change is closely associated with the irreversible coloring in WO_3-3. Evidently, the accelerated harsh voltammetric cycling procedure leads to deterioration of the WO_3-3 films' morphology. In contrast, for WO_3-2, from ECD2 after convential long-term voltammetric cycling, a less porous morphology with even smaller particles than WO_3-1 is presented. Thereby, surface analysis reveals that two cycling protecoles will give two different micro evolutions in WO_3 films. For NiO thin films, NiO-1 and NiO-3 display unambiguous particles (see SEM graphs) in accordance with the crystallinity feature induced in XRD. After convential long-term CV cycling, the particle distribution in NiO-2 micrograph is getting more uneven, which means they tend to be clustered in certain areas as exhibited in 3D AFM figure. For NiO-3, the harsh electrochemical cycling also results in the agglomeration development.

Moreover, in the SEM figures for uncycled NiO-1 and degraded NiO-2 and NiO-3 films, there are significant macroscopic cracks, which tend to expand in the degradation process. These cracks will increase the permeability of the electrode, and at the same time, decrease the homogeneity of charge transfer due to the unevenness of the surface. These changes would induce a reduction of the cycling life, which is a fatal flaw of the ECDs. What is more, excess cracks will lead to deterioration of the film's microstructure, and the adhesion between Ni oxide grains and between film and

substrate will become weak. The weak mechanical adhesion will make the film peel off from the substrate at last.[4]

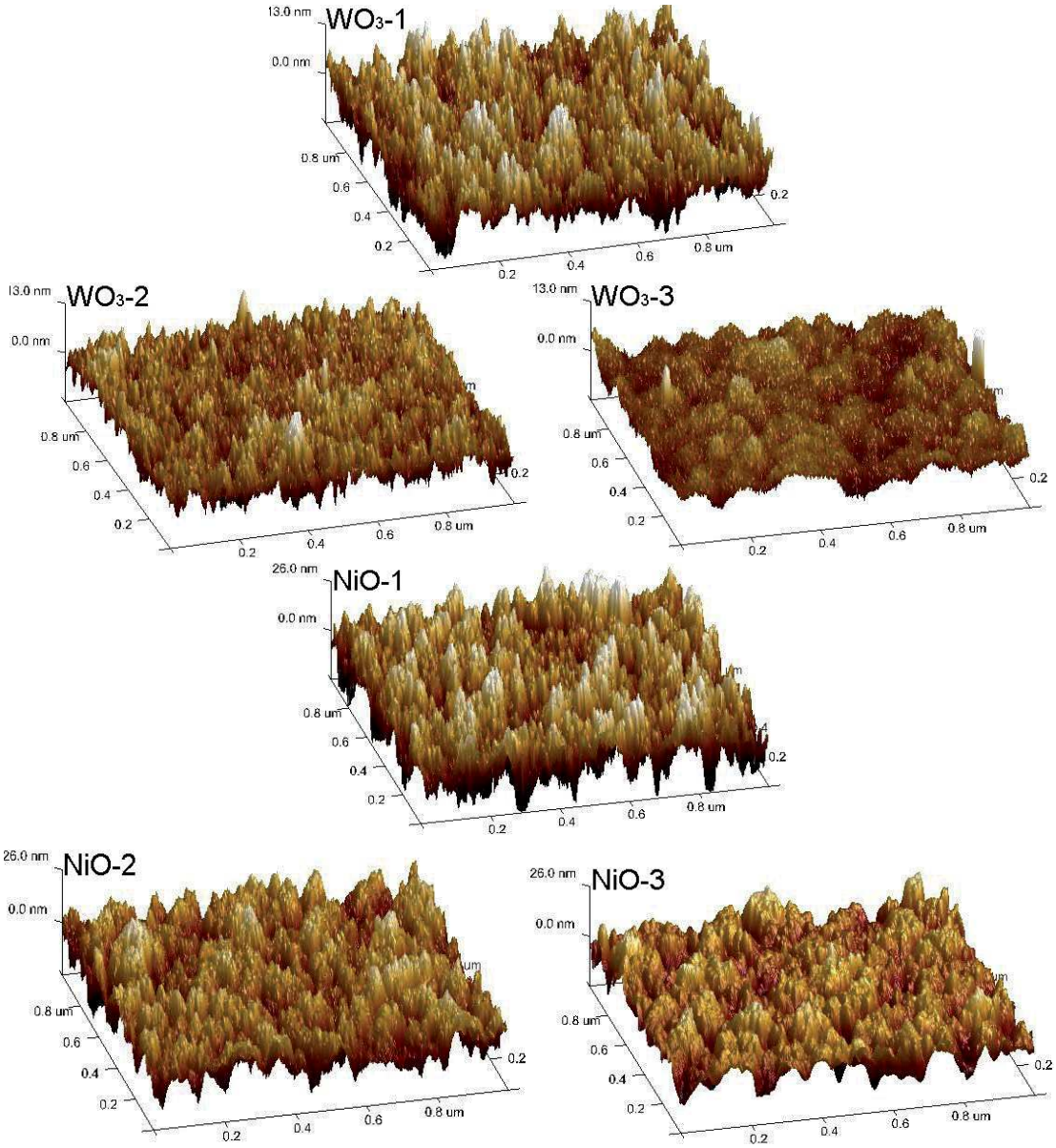

Fig. S5 Three dimensonal AFM images for WO_3 and NiO films.

4. O1s peak analysis of X-ray photoelectron spectroscopy

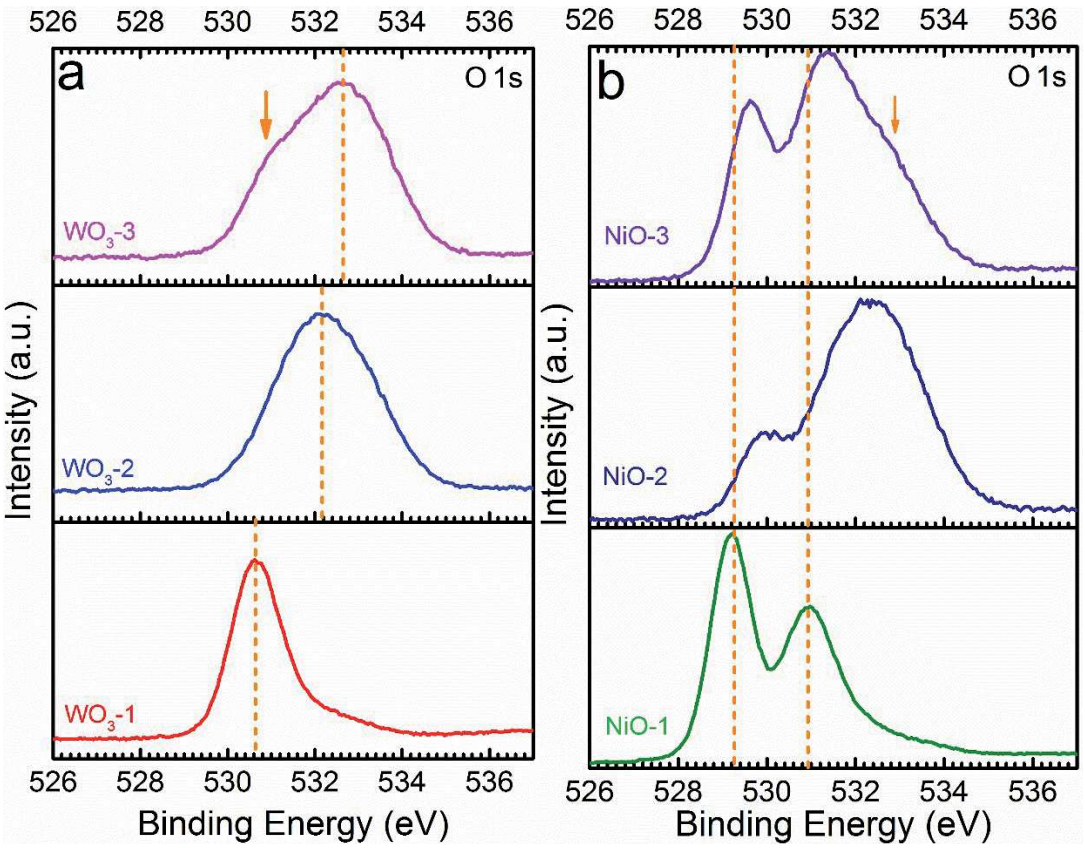

Fig. S6 XPS spectrum comparison of O1s peak of electrochromic films degraded in various cycling protocles.

XPS spectrum of O1s demonstrate that the sample contains W as well as Ni oxide in respect with the W4f and Ni2p analysis. In Fig. S6 (a) the scan of W oxide exhibits a sharp and asymmetric peak at 530.6 eV for bare WO_3-1 and a shifted broad peak for degraded WO_3-3. The peak broadening and shifting towards higher binding energy direction in O 1s XPS profile indicate that W^{5+} in matrix films is partly oxidized chemically. Another significant effect on NiO lies in the change of the relative intensity ratio of the two main peak in the O 1s scan as demonstrated in panel b. This change is more related to the relative concentration of Ni^{2+} and Ni^{3+}.[3] The increased complexity in degraded films is reflected by the shoulder of the main peak, as marked by the arrow in the figure. The increase in Ni^{3+} percentage in degraded films is also evidenced by XPS Ni 2p analysis. The O1s peaks of all the NiO based films mainly include two components, *i.e.* the left peak (LP) and the right peak (RP). The degraded NiO-2 and NiO-3 samples show significant peak shift towards higher binding energy direction as well as peak broadening, in accordance with the analysis of Ni $2p_{3/2}$ spectra, which is

attributed to the large amount of Li^+ ions trapping. Moreover, the relative intensity ratio of RP/LP increases for degraded films and it adds the complexity in analyzing, mainly due to the formation of Li_2O and/or the compound in $Ni_{1-x}O$-Li_2O system. Here, we cannot go too far or determine what the specific compound is.

References

[1] Bueno, P.R. Pontes, F.M. Leite,E.R. Bulhões, L.O.S. Pizani, P.S. Lisboa-Filho, P.N. Schreiner, W.H. Structural Analysis of Pure and $LiCF_3SO_3$-Doped Amorphous WO_3 Electrochromic Films and Discussion on Coloration Kinetics. *J. Appl. Phy.* **2004**, *96*, 2102-2109.

[2] Kitao, M. Izawa, K. Urabe, K. Preparation and Electrochromic Properties of RF-Sputtered NiO_x Films Prepared in $Ar/O_2/H_2$ Atmosphere. *Jpn. J. Appl. Phys.* **1994**, *33.12*, 6656.

[3] Wang, M. Thimont, Y. Presmanes, L. Diao, X. Barnabé, A. The Effect of the Oxygen Ratio Control of DC Reactive Magnetron Sputtering on As-Deposited Non Stoichiometric NiO Thin Films. *Appl. Surf. Sci.* **2017**, *419*, 795-801.

[4] R.T. Wen, C.G. Granqvist, G.A. Niklasson, *ChemElectroChem,* 2016, **3**, 266-275.